

NUMERICAL EXPERIMENTS ON FINE STRUCTURE WITHIN RECONNECTING CURRENT SHEETS IN SOLAR FLARES

CHENGCAI SHEN^{1,2}, JUN LIN^{1,3}, AND NICHOLAS A. MURPHY³

¹ Yunnan Astronomical Observatory, Chinese Academy of Sciences, P.O. Box 110, Kunming, Yunnan 650011, China

² Graduate School of the Chinese Academy of Sciences, Beijing 100039, China

³ Harvard-Smithsonian Center for Astrophysics, 60 Garden Street, Cambridge, MA 02138, USA

Received 2011 February 4; accepted 2011 May 15; published 2011 July 22

ABSTRACT

We perform resistive magnetohydrodynamic simulations to study the internal structure of current sheets that form during solar eruptions. The simulations start with a vertical current sheet in mechanical and thermal equilibrium that separates two regions of the magnetic field with opposite polarity which are line-tied at the lower boundary representing the photosphere. Reconnection commences gradually due to an initially imposed perturbation, but becomes faster when plasmoids form and produce small-scale structures inside the current sheet. These structures include magnetic islands or plasma blobs flowing in both directions along the sheet, and X-points between pairs of adjacent islands. Among these X-points, a principal one exists at which the reconnection rate reaches maximum. A fluid stagnation point (S-point) in the sheet appeared where the reconnection outflow bifurcates. The S-point and the principal X-point (PX-point) are not co-located in space though they are very close to one another. Their relative positions alternate as reconnection progresses and determine the direction of motion of individual magnetic islands. Newly formed islands move upward if the S-point is located above the PX-point, and downward if the S-point is below the PX-point. Merging of magnetic islands was observed occasionally between islands moving in the same direction. Reconnected plasma flow was observed to move faster than blobs nearby.

Key words: instabilities – magnetic reconnection – magnetohydrodynamics (MHD) – methods: numerical – plasmas – Sun: flares

Online-only material: animations

1. INTRODUCTION

The energy release involved in a solar eruption is violent, and a huge amount of energy (up to 10^{32} erg), magnetic flux (up to 10^{22} Mx), and plasma (up to 10^{16} g) flows into the outermost corona and interplanetary space. Several flare models in which a magnetic reconnection current sheet connects a flare to a coronal mass ejection (CME) have been developed in the past 40 years. The first one was suggested by Carmichael (1964), and it was later developed by Sturrock (1968), Hirayama (1974), and Kopp & Pneuman (1976) into the well-known Kopp–Pneuman model, or the CSHKP model. It was further developed by Martens & Kuin (1989) and Lin & Forbes (2000) to the catastrophe model of solar eruptions in which the eruption produces a CME and an associated flare connected to one another through a long current sheet. In the catastrophe model, the magnetic field is severely stretched to form an effectively open magnetic configuration including a neutral sheet separating magnetic fields of opposite polarity. Magnetic reconnection occurring inside the current sheet creates growing flare loops in the corona and separating flare ribbons on the solar disk, and helps CMEs propagate outward smoothly (e.g., see Forbes 2000; Forbes & Lin 2000; Lin & Forbes 2000; Lin 2002; Lin et al. 2003).

The CME/flare current sheet dynamically forms and develops in the eruptive process. It becomes long and thin as the CME moves into interplanetary space. Consequently, the sheet could become unstable to several magnetohydrodynamic (MHD) instabilities. Among these instabilities, the tearing mode is most important and has been extensively studied. It was investigated for the first time by Furth et al. (1963), who showed that it occurs on the timescale τ , such that $\tau_A < \tau < \tau_d$. Here $\tau_d = l^2/\eta$ and $\tau_A = l/v_A$ are the times it takes to traverse the sheet at

the diffusion speed $v_d = \eta/l$ and at the Alfvén speed v_A , respectively, and it has the effect of creating many small-scale magnetic islands in the sheet. When the tearing mode occurs, the current sheet can tear along current flow lines, forming a chain of filaments or magnetic islands. In other words, resistive instabilities produce current eddies in current sheets. Subsequently, the eddies and associated magnetic islands dissipate, releasing magnetic energy in the process.

In observations, many events have reportedly caused long current sheets to develop in CME/flare processes (e.g., see Ciaravella et al. 2002; Ko et al. 2003; Raymond et al. 2003; Lin et al. 2005; Bemporad et al. 2006; Ciaravella & Raymond 2008). Small plasmoids or magnetic islands were found to flow along the current sheet either sunward or anti-sunward (e.g., see Sheeley & Wang 2002; Innes et al. 2003; Ko et al. 2003; Raymond et al. 2003; Sheeley et al. 2004; Asai et al. 2004; Lin et al. 2005; Vršnak et al. 2009; Milligan et al. 2010; Nishizuka et al. 2010). Recently, Savage et al. (2010) studied an event occurring on 2008 April 9, which was observed by *TRACE*, *Hinode*/XRT, and *SOHO*/LASCO. The event developed a long CME/flare current sheet in which magnetic reconnection outflows were well observed. What is especially nice about this work is that both sunward and anti-sunward reconnection outflows were observed simultaneously and that the anti-sunward outflow is well tracked from the lower corona in the *Hinode*/XRT field of view out to the corona in the LASCO/C2 field of view.

In numerical experiments, formation and evolution of plasma blobs in the current sheets in solar flares and CMEs have also been noted for two decades. The results of Forbes & Malherbe (1991) and Riley et al. (2007) suggested the tearing mode instability plays an important role in magnetic field diffusion and governing the scale of the sheet. Bárta et al. (2008) reported

a broad variety of the kinematical/dynamical properties of plasmoids. In their simulations, a plasmoid can move upward, downward, or may even change the direction of its motion.

Recently, similar processes related to plasmoids inside extended current sheets have been studied extensively in the plasma physics community as well. Loureiro et al. (2007) and Ni et al. (2010) established that high Lundquist number current sheets are unstable to the formation of plasmoids. Resistive MHD simulations have confirmed and further investigated the scaling of this instability (Samtaney et al. 2009; Bhattacharjee et al. 2009; Huang & Bhattacharjee 2010; Skender & Lapenta 2010; Bettarini & Lapenta 2010; Uzdensky et al. 2010). The formation of plasmoids leads to a reconnection rate much faster than predicted by the Sweet–Parker model. However, Shepherd & Cassak (2010) argue that collisionless effects, which become important on scales comparable to the ion inertial length, are needed to explain the observed reconnection rates. Secondary island formation is also observed during particle-in-cell simulations of elongated current sheets (e.g., Daughton et al. 2006).

In this work, we investigate how and at what threshold plasma blobs form in CME/flare current sheets. We perform a detailed investigation of various properties of plasma blobs via two-dimensional MHD simulations using the SHarp and Smooth Transport Algorithm (SHASTA; Boris & Book 1973, 1976; Weber et al. 1979) code that is publicly available. This code is an explicit, flux-corrected transport code originally developed by Boris & Book (1973, 1976), and later modified by Weber et al. (1979) to include magnetic diffusion. We further modify and improve the SHASTA code by either using the adaptive mesh refinement (AMR) technique or by simply increasing grid points in calculations so that our results can have much higher resolution and reveal more details about the internal structures of the sheet and the reconnection process. In Section 2, we describe the physical model and how the original SHASTA code is modified and improved for our simulations. The numerical results are presented in Section 3. The discussion and conclusions are given in Section 4.

2. DESCRIPTIONS OF THE MODEL AND THE NUMERICAL METHOD

This work could be considered a follow-up to that of Forbes & Malherbe (1991) who utilized the SHASTA code to study the magnetic reconnection process in the two-ribbon flare for the first time. The initial structure of the magnetic field investigated in this work is in mechanical and thermal equilibrium and is shown in Figure 1, which is used to model the Kopp–Pneuman configuration of a two-ribbon flare that results from the loss of equilibrium in the coronal magnetic field (e.g., see Kopp & Pneuman 1976; Cargill & Priest 1982; Švestka & Cliver 1992; Forbes 2000; Lin et al. 2003).

2.1. Basic Equations Governing the Evolution

The system commences to evolve due to the attraction of the magnetic fields of opposite polarity at two sides of the current sheet, leading them to approach one another and to squeeze the sheet. The process is governed by the resistive MHD equations as follows:

$$\frac{\partial \rho}{\partial t} + \nabla \cdot (\rho \mathbf{v}) = 0, \quad (1)$$

$$\rho \left[\frac{\partial}{\partial t} + (\mathbf{v} \cdot \nabla) \right] \mathbf{v} = -\nabla p + \mathbf{J} \times \mathbf{B}, \quad (2)$$

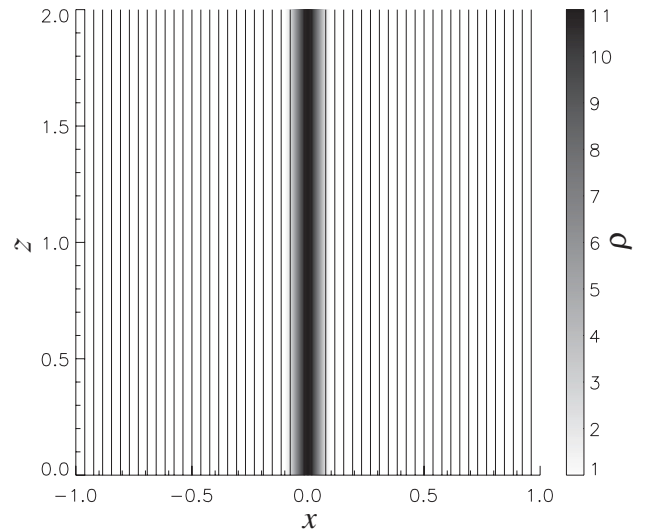


Figure 1. Initial configuration of the magnetic field and the distribution of the plasma density on the x - z plane. The solid line is for the magnetic field line, and the gray scale is for the density.

$$\frac{\partial \mathbf{B}}{\partial t} = \nabla \times (\mathbf{v} \times \mathbf{B}) + \eta_m \nabla^2 \mathbf{B}, \quad (3)$$

$$\frac{\rho^\gamma}{\gamma - 1} \left(\frac{\partial}{\partial t} + \mathbf{v} \cdot \nabla \right) \frac{p}{\rho^\gamma} = \mu_0 \eta_m J^2, \quad (4)$$

$$p = \frac{1}{\tilde{\mu}} \tilde{R} \rho T, \quad (5)$$

$$\mathbf{J} = \frac{1}{\mu_0} \nabla \times \mathbf{B}, \quad (6)$$

which include the mass continuity equation, the momentum equation, the magnetic induction equation, the energy equation, the universal gas law, and Ampere’s law. The quantities ρ , \mathbf{v} , \mathbf{B} , p , \mathbf{J} , and T are mass density, flow velocity, magnetic field, gas pressure, electric current density, and temperature, respectively; and η_m , γ , μ_0 , and \tilde{R} are the magnetic diffusivity, the ratio of specific heats, the magnetic permeability of free space, and the universal gas constant, respectively. In addition to the above equations, magnetic field \mathbf{B} is subject to the divergence-free condition as well

$$\nabla \cdot \mathbf{B} = 0. \quad (7)$$

Normalization of the above important quantities brings \mathbf{B} , ρ , p , and \mathbf{v} to the following dimensionless form:

$$\begin{aligned} \mathbf{B}' &= \frac{\mathbf{B}}{B_0}, & \rho' &= \frac{\rho}{\rho_0}, & p' &= \frac{p}{B_0^2/\mu_0}, \\ \mathbf{v}' &= \frac{\mathbf{v}}{v_0}, & T' &= \frac{\beta_0 T}{2T_0}, & J' &= \frac{J}{J_0} \end{aligned} \quad (8)$$

with

$$v_0 = B_0/\sqrt{\mu_0 \rho_0}, \quad J_0 = \frac{B_0}{\mu_0 L}, \quad \text{and} \quad \beta = 2\mu_0 p_0/B_0^2, \quad (9)$$

where ρ , \mathbf{v} , \mathbf{B} , and p are the variables with dimensions, those with prime ($'$) are the corresponding dimensionless variables, and ρ_0 , B_0 , T_0 , L , and v_0 are the initial mass density, magnetic field, temperature, width of the simulation domain, and Alfvén speed of the ambient background plasma, respectively. The

dimensionless time t' and spatial coordinates x' and z' are related to their dimensional counterparts by

$$x' = \frac{x}{L}, \quad z' = \frac{z}{L}, \quad t' = \frac{t}{t_0}, \quad (10)$$

where $t_0 = L/v_0$ is the Alfvén timescale with respect to L . In our calculations below, the above characteristic values are taken as follows:

$$B_0 = 10 \text{ G}, \quad T_0 = 10^6 \text{ K}, \quad \rho_0 = 2.9 \times 10^{-15} \text{ g cm}^{-3},$$

and $L = 10^5 \text{ km}$, (11)

which lead to $\beta = 0.1$, $v_0 \approx 525 \text{ km s}^{-1}$, and $t_0 \approx 190 \text{ s}$.

Rewriting Equations (1) through (6) in dimensionless form, we have

$$\frac{\partial \rho}{\partial t} + \nabla \cdot \rho \mathbf{v} = 0, \quad (12)$$

$$\rho \left[\frac{\partial \mathbf{v}}{\partial t} + (\mathbf{v} \cdot \nabla) \mathbf{v} \right] = -\nabla p + \mathbf{J} \times \mathbf{B}, \quad (13)$$

$$\frac{\partial \mathbf{B}}{\partial t} = \nabla \times (\mathbf{v} \times \mathbf{B}) + \frac{1}{R_m} \nabla^2 \mathbf{B}, \quad (14)$$

$$\frac{\rho^\gamma}{\gamma - 1} \left(\frac{\partial}{\partial t} + \mathbf{v} \cdot \nabla \right) \frac{p}{\rho^\gamma} = \mu_0 \frac{1}{R_m} J^2, \quad (15)$$

$$p = \rho T, \quad (16)$$

$$\nabla \cdot \mathbf{B} = 0. \quad (17)$$

Here, $R_m = v_0 L / \eta_m$ is the magnetic Reynolds number based on the characteristic length L and the Alfvén speed v_A . We note here that the prime (') of each dimensionless variable has been ignored in the above equations for simplicity, and any variable appearing hereafter is dimensionless. Equations (12) through (15) will be solved by the SHASTA code in which magnetic vector potential \mathbf{A} is involved such that

$$\frac{\partial \mathbf{A}}{\partial t} + \nabla \cdot (\mathbf{A} \mathbf{v}) = \mathbf{A} \nabla \cdot \mathbf{v} + R_m^{-1} \nabla^2 \mathbf{A} \quad (18)$$

is used to replace Equation (14) to ensure that condition (17) always holds in our calculations. Here \mathbf{A} is related to \mathbf{B} in the way of $\mathbf{B} = \nabla \times \mathbf{A}$. In the two-dimensional case, this becomes $\mathbf{B} = \nabla \times A \hat{\mathbf{y}}$ with A being the y -component of \mathbf{A} and $\hat{\mathbf{y}}$ being the unit vector in the y -direction. Specifically, we have replaced the two separate diffusive equations for B_x and B_z in Weber's SHASTA code by a single diffusive equation for A , and there are two subroutines which compute A from \mathbf{B} and \mathbf{B} from A (see also the discussions of Forbes & Malherbe 1991).

Under such an arrangement for the magnetic field and vector potential, we are able to write the initial and boundary conditions for solving Equations (12) through (17). The initial configuration shown in Figure 1 includes a vertical current sheet that separates two magnetic fields of opposite polarity, and is line-tied to the bottom boundary surface. It is described mathematically by

$$\begin{aligned} B_z(x, z, t = 0) &= x/|x|, \quad \text{for } |x| > w, \quad \text{and} \\ B_z(x, z, t = 0) &= \sin(\pi x/2w), \quad \text{for } |x| \leq w. \\ B_x(x, z, t = 0) &= 0, \\ \mathbf{v}(x, z) &= 0, \\ \rho(x, z, t = 0) &= (\beta + 1 - B^2)/\beta \\ p(x, z, t = 0) &= T\rho(x, z, t = 0) = \beta\rho(x, z, t = 0)/2, \end{aligned} \quad (19)$$

where w is the half-width of the current sheet, and all parameters in Equation (19) are dimensionless.

The boundary conditions are arranged in this way: the right, left, and top sides of the simulation domain are the open or the free boundary on which the plasma and the magnetic flux are allowed to enter or exit freely and the boundary at the bottom ensures that the magnetic field is line-tied,

$$\frac{\partial A(x, 0, t)}{\partial t} = 0, \quad (20)$$

and the plasma does not slip and is fixed to the wall,

$$\mathbf{v}(x, 0, t) = \mathbf{0}, \quad (21)$$

respectively. Combining boundary conditions (20) and (21) with the initial conditions in Equation (19), we found

$$\left. \frac{\partial p(x, z, t)}{\partial z} \right|_{z=0} = 0 \quad \text{and}$$

$$\left. \frac{\partial \rho(x, z, t)}{\partial z} \right|_{z=0} = 0.$$

Since $\partial A / \partial t = -v_x B_z - \eta_m J$, Equations (20) and (21) require that J vanish on the bottom boundary as well, namely,

$$J(x, 0, t) = 0 \quad \text{for } t > 0.$$

The evolution in the system of interest starting with the configuration shown in Figure 1 can be studied via solving Equations (12) through (17) with conditions (19) through (21). The modified SHASTA code is used to solve these equations after several necessary tests. We describe the code and the test in the next section.

2.2. The Modified SHASTA Code and the Efficiency Test

The SHASTA code is well suited for studying shock waves since it can sustain a sharp shock transition over only two or three mesh points, and shock transitions in the code are free from spurious oscillations caused by Gibb's phenomenon. The original SHASTA code solves the resistive MHD equations in a conservative form (see below) so that quantities such as mass, momentum, magnetic flux, and total energy are normally conserved to high accuracy (<1% error). However, large errors are sometimes generated in the pressure and temperature if the plasma β is greatly different from unity. These errors can be reduced if the conservative form of the energy equation is replaced by an energy equation for the pressure. Therefore, the conservation of the total energy was not maintained as well as other parameters.

A revised version made by Weber et al. (1979) computes diffusion implicitly using a standard tridiagonal matrix procedure for parabolic equations. When the diffusion is computed the advective terms are excluded, and similarly when the advection is computed the diffusive terms are excluded. As long as the time steps are small compared to the physical timescales, the results are the same as if both sets of terms had been solved simultaneously.

Using the SHASTA code revised by Weber et al. (1979), Forbes & Malherbe (1991) performed numerical experiments of magnetic reconnection and radiative cooling that may take place in the two-ribbon flare process. They noticed that the tearing mode did occur in the sheet and played an apparent role

Table 1
Values of Parameters for Different Cases

Case	N_g	R_m	N_{AMR}
1	103×201	5.0×10^2	2
2	151×301	1.0×10^4	0
3	151×301	1.0×10^4	2
4	151×301	5.0×10^4	2
5	301×601	5.0×10^4	0
6	301×601	5.0×10^5	2

in diffusing the magnetic field. Many plasma blobs resulting from the tearing mode were recognized, and the development of the instability in the linear stage duplicated the results of Furth et al. (1963) in theory, but when the evolution began to develop non-linearly, deviations were seen. However, the low resolution of the grid prevented them from further investigating the case of high R_m and low β .

With the improvement in computational hardware and the available resources, Shen & Lin (2009, 2010) further modified and improved SHASTA by implementing AMR so that a case of a large magnetic Reynolds number (up to 5×10^4) and small plasma β (~ 0.1) could be studied smoothly. In the present work, we perform more tests and choose an appropriate approach for investigating the reconnection process in the two-ribbon flare.

Several cases are considered with different combinations of some parameters in addition to those arranged above. These parameters include the initial grid number of the experiment domain in each case, N_g , magnetic Reynolds number, R_m , and the number of refinements of the initial grids via AMR, N_{AMR} . They are listed in Table 1 for six cases, and the initial values for the plasma β and the half-width of the current sheet, w , are taken as 0.1 for all cases. In these cases, refinement by AMR was conducted for cases 1, 3, 4, and 6, and the refining times $N_{\text{AMR}} = 2$ for all these four cases (see values of N_{AMR} listed in Column 4 of Table 1). For cases 2 and 5, on the other hand,

no AMR refinement was conducted. In calculations below R_m ranges from 5×10^2 to 5×10^5 , and calculations are performed only in the region of $x > 0$ because of the symmetry in the configuration. Figure 2 displays some results of our tests for different cases.

For the low R_m case, for example, case 1 ($R_m = 500$), reconnection quickly sets in through almost the whole current sheet even when the sheet is still thick, and formation of an X-point in the sheet becomes apparent after a group of magnetic arches (loops) has been created (see also Shen & Lin 2009). Figure 2(a) shows the current density distribution and the magnetic configuration at time $t = 24.0$ for this case. The AMR technique ($N_{\text{AMR}} = 2$) is used and calculations in the experiment run smoothly. As a result of low R_m , the magnetic field can be dissipated at a fast rate in the whole current sheet, so no magnetic island develops in the sheet. As the AMR technique was applied, some fine features, including a termination shock (see also discussions of Forbes & Malherbe 1991 for more details), on the top of the loop system can be well recognized.

As R_m increases, reconnection apparently becomes difficult in a thick current sheet. In the case of higher R_m and lower grid resolution without refinement, for example, case 2 ($N_g = 151 \times 301$ and $N_{\text{AMR}} = 0$ as shown in Table 1), the calculation quickly breaks down as the sheet gets thinner, and the experiment stops. With application of the AMR technique ($N_{\text{AMR}} = 2$), on the other hand, the calculation was immediately stabilized (case 3), and fast reconnection commences when the sheet gets thin enough and magnetic islands form (see Figure 2(b)). This suggests that the AMR technique helps stabilize the calculation to a certain extent, and formation of the magnetic islands inside the sheet indicates the beginning of the tearing mode instability (e.g., see Furth et al. 1963). The tearing mode produces many magnetic islands, or plasmoids or plasma blobs, inside the current sheet, and the reconnection outflow moves these small structures either upward or downward depending on when and

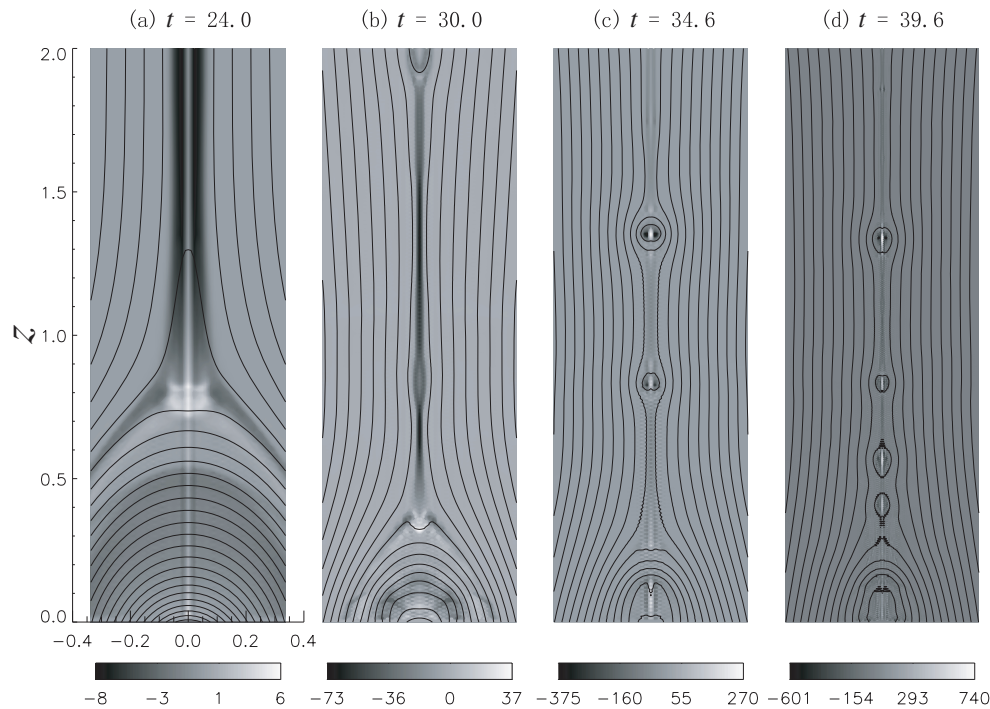


Figure 2. Contours of J (gray scale) and magnetic field (continuous curves) for different cases as specified in Table 1: (a) case 1 for $t = 24.0$, (b) case 3 for $t = 30.0$, (c) case 4 for $t = 34.6$, and (d) case 6 for $t = 39.6$. The gray bar below each panel indicates the value of J .

where individual blobs form. We shall see later that magnetic islands are more likely to appear in the reconnection process occurring in high R_m environments.

With much bigger R_m , for instance, $R_m = 5 \times 10^4$ in cases 4 and 5, a much smaller grid size and shorter time step are required to maintain the stability of calculations. We perform our tests in different approaches for these two cases. In case 4, we start calculations with a lower grid resolution ($N_g = 151 \times 301$ and $N_{\text{AMR}} = 2$) and apply the AMR technique to calculations and in case 5, we start with a higher but fixed grid resolution ($N_g = 301 \times 601$ and $N_{\text{AMR}} = 0$). As expected, the experiments in both cases run smoothly and give similar evolutionary pictures of the magnetic reconnection process: the current sheet continues to become thinner as evolution in the system commences. Not until the thickness w decreases to about $1/20$ of its initial value do the characteristics of the tearing mode instability begin to appear, namely, the appearance of multiple magnetic islands in the sheet. Figure 2(c) displays the magnetic configuration and the current contours at time $t = 34.6$ for case 4, which clearly manifests two magnetic islands in the sheet.

Furthermore, we increase R_m to 5×10^5 with higher grid resolution, $N_g = 301 \times 601$, and AMR, $N_{\text{AMR}} = 2$, in case 6. Fast reconnection becomes more difficult to start, and the sheet gets much thinner than previous cases before magnetic islands form. Figure 2(d) shows the magnetic configuration and distribution of J for case 6 at $t = 39.6$. A lot of magnetic islands are seen to form along the current sheet, but numerical errors also create obvious disturbances to both the field and J . This suggests that the power of AMR may have reached its maximum at $R_m = 5 \times 10^5$ for the SHASTA code. However, we also tried increasing the grid resolution to $N_g = 601 \times 901$ and found that the experiment breaks down midway through calculations. We thus realize that the SHASTA code may not be able to deal well with cases of $R_m > 10^5$, regardless of whether AMR or very high grid resolution is used. Hence, we stay with the parameter combination for case 5 in our calculations below in order to avoid extra errors and to be sure that the experiment results are reliable.

Before ending this section, we should note two things. First of all, numerical diffusion is inevitable in any numerical experiment, whether or not AMR is used. Even different levels of AMR may effectively cause different levels of numerical diffusion, yielding numerical noise in our results. To identify the numerical noise, we perform an estimate as below.

The magnetic induction equation (Equation (14)) can be written as

$$\frac{\partial A}{\partial t} = (\mathbf{v} \times \mathbf{B})_y - \frac{J}{R_m} \quad (22)$$

in two dimensions. In the absence of numerical diffusion, both sides of Equation (22) should ideally balance with each other. In the realistic numerical experiment, on the other hand, an error exists such that the two sides do not balance each other as a result of the numerical diffusion. The behavior of this error can be studied by comparing the difference of the values of two sides near the current sheet for specific cases. We conduct this comparison for the parameters adjacent to the current sheet because the numerical diffusion in this region reaches maximum.

Suppose we define $a \equiv \partial A / \partial t$ and $b \equiv (\mathbf{v} \times \mathbf{B})_y - J / R_m$, and we calculate a and b near the principal X-point (PX-point) for cases 4 and 5 over the time interval between $t = 10$ and $t = 25$, then estimate three kinds of relative difference between a and b : $|a - b|/|a|$, $|a - b|/|b|$, and $2|a - b|/|a + b|$, respectively. The

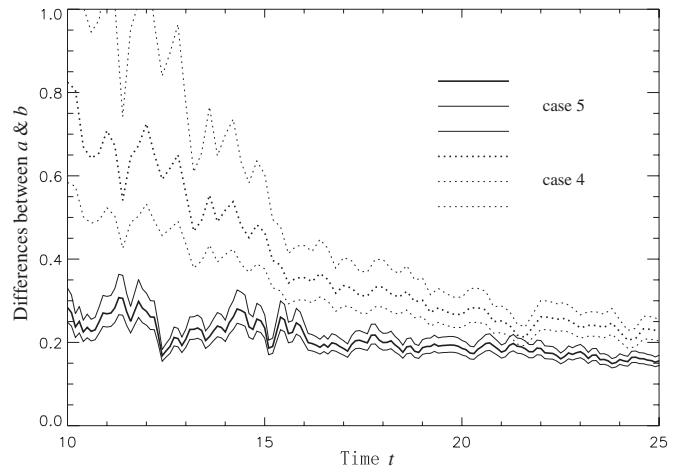


Figure 3. Three kinds of relative differences between a and b , where a is the value of the left side of Equation (22) and b is that of the right side. Dotted curves are for case 4 and solid curves for case 5. The variety of each symbol sizes from thin to thick are for $|a - b|/|a|$, $|a - b|/|b|$, and $2|a - b|/|a + b|$, respectively.

results are plotted in Figure 3, in which dotted curves are for case 4, solid curves for case 5, and various sizes of each symbol are for various relative differences between a and b . As expected, none of these results is zero, which apparently suggests existence of the error due to numerical diffusion. However, the behavior of these errors varies from case to case. In case 4, the grid resolution is low initially, so the errors are fairly large at the beginning. As AMR functions properly, we see that all three errors decrease to about 20% continuously until the pre-set upper limit of the AMR level is reached. In case 5, the AMR function is turned off, but the initial resolution is high. Therefore, the error due to numerical diffusion is controlled at a low level of around 20% and is roughly kept at this level over the whole period of the test.

Overall, Figure 3 suggests that the error caused by numerical diffusion is not large when the calculation is in steady progress in both cases 4 and 5. For the fixed grid size of high resolution, this error is controlled at a low level from the very beginning. If the initial resolution of the grid is low but AMR functions properly, however, the error is rather large at the beginning but is eventually suppressed to a low level. In our cases, this error is about 20% as the experiment progresses steadily, namely, the numerical noise included in our results is at the level of about 20% of the physical signal.

Another aspect we need to note is that the information revealed by the above tests indicates that the performance of a code for the given computational resources, with or without AMR, is sensitive to the magnetic Reynolds number R_m . In the case of small R_m in an apparent way, for example, case 1, the code always runs smoothly with low grid resolution (small N_g) and a low level of the AMR technique (small N_{AMR} or even $N_{\text{AMR}} = 0$), and no significant features of turbulence occur inside the current sheet (see also Figure 4(a) as well as the results of Forbes & Malherbe 1991). As R_m increases, however, running the code properly becomes tricky and difficult, and high initial grid resolution or a high AMR level is required. However, comparing the results of cases 2 through 5 with one another suggests the trade-off between N_g and N_{AMR} such that large N_g is required if the level of AMR is low (namely, small N_{AMR}) and selecting N_g and N_{AMR} or their combination is determined by R_m for the specific case.

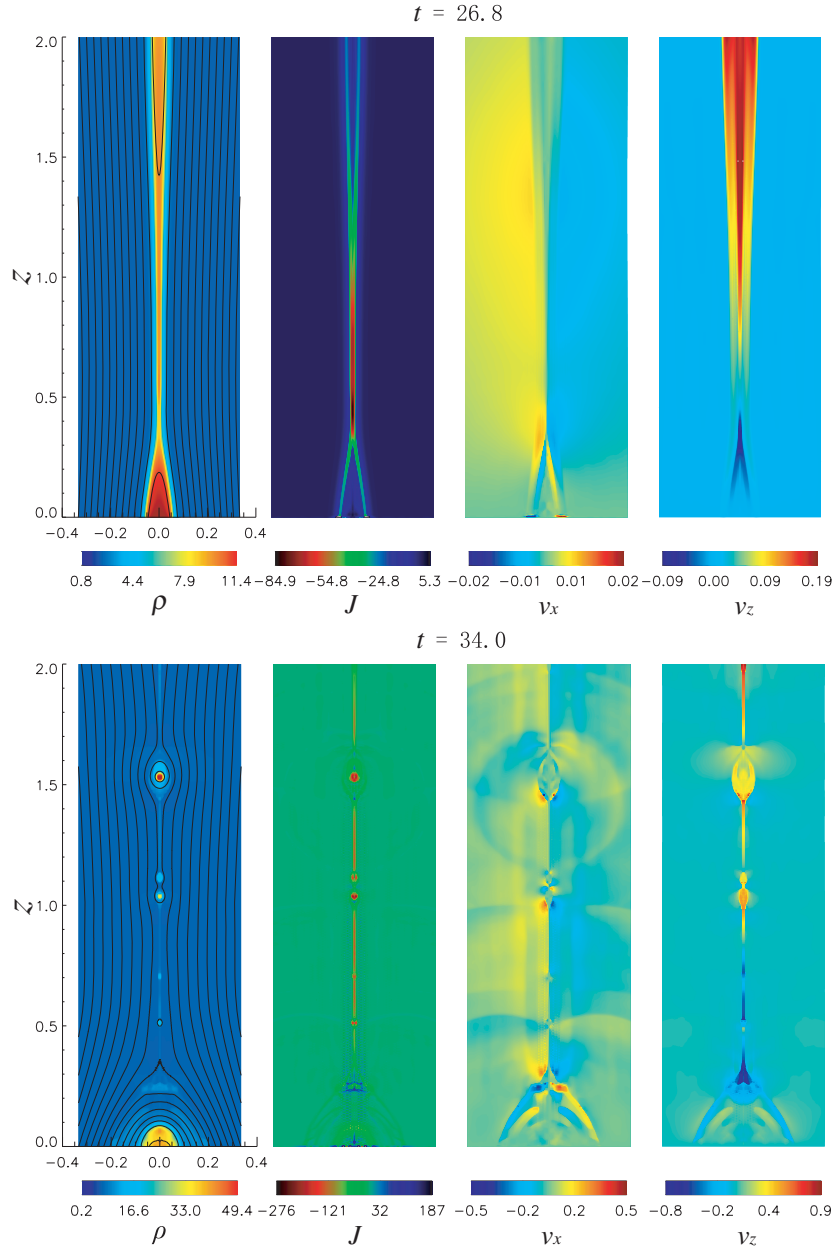


Figure 4. Contours of magnetic field (continuous curves) and ρ (color scale, left), J (middle left), v_x (middle right), and v_z (right) at $t = 26.8$ (upper row) and $t = 34.0$ (lower row).

(An animation of this figure is available in the online journal.)

3. RESULTS OF NUMERICAL EXPERIMENTS

With a small perturbation added to the current sheet, the magnetic configuration displayed in Figure 1 begins to evolve, and the magnetic fields at two sides of the current sheet move toward one another due to the attraction between the fields of opposite polarity. This squeezes the sheet, and the sheet narrows until it becomes thin enough that the tearing mode and other instabilities take place (e.g., see Furth et al. 1963; Loureiro et al. 2007; Ni et al. 2010) inside it. Many magnetic islands appear in the sheet, and the consequent fast reconnection results in the formation and growth of closed field lines where the flare loops are supposed to lie (see Figure 4 and the associated movie). Multiple X-points appear between every pair of islands. Among these X-points exists a principal one at which the rate of reconnection reaches maximum. Very close to the PX-point exists a flow

stagnation point (S-point) at which the instantaneous plasma velocity vanishes in the simulation reference frame. Detailed analyses of these features are provided below.

3.1. Evolution in the Current Sheet

The current sheet shown in Figure 1 is about 10 times denser than its surroundings. At an early stage of evolution, the equilibrium in the system breaks down as a result of the initial perturbation imposed on the system. Plasma and magnetic fields on the two sides of the sheet commence to move to one another gradually, causing the sheet to become thinner, but the current sheet does not fragment until evolution reaches the stage at $t = 26.8$ when the sheet is already very thin because of the high value of R_m (5×10^4). As discussed in Section 2, the thinning process is sensitive to the value of R_m . In the low R_m condition,

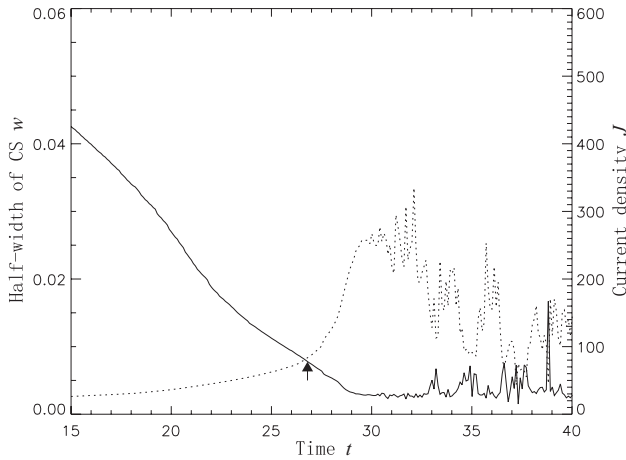


Figure 5. Variations of w (solid curve) and J (dotted curve) near the PX-point vs. time. The arrow specifies the time $t = 26.8$ when the first magnetic island (O-point) starts to form.

the current sheet diffuses fast enough and no plasmoid forms inside the sheet. Previous numerical experiments indicated that the threshold ratio of the length-to-thickness of the sheet, 2π , for the tearing mode given by Furth et al. (1963) should be the lower limit. In these experiments, the value of this ratio may exceed 50 before the plasmoids begin to form (e.g., see Ni et al. 2010 and references therein). On the other hand, our experiments show that the evolution of the current sheet represented by the decrease in the sheet thickness $2w$ is not uniform along the current sheet. Instead squeezing of the sheet due to the plasma inflow mainly occurs at a specific location at around $z = 0.48$ from which the first X-point forms at $t = 23.0$. We shall notice later that this X-point eventually becomes the principal one, namely, the PX-point.

We focus on the evolution of the current sheet at the PX-point. We plot values of w near the PX-point versus t within the time interval between $t = 15.0$ and $t = 40.0$ in Figure 5 (see the solid curve). In the early phase, the half-width of the current sheet w , which has the initial value 0.1, continues to decrease slowly. At $t = 26.8$ when the first magnetic island starts to form, w has decreased to 0.0075. After time $t = 26.8$, w gradually decreases to the minimum value 0.0025 and it subsequently fluctuates around this minimum value. We shall see later that this oscillating behavior is related to the formation of multiple X- and O-points in the sheet.

At the same time, the electric current density J inside the sheet evolves as well. Initially, its maximum value at the center of the sheet is around 26. It increases gradually as w decreases. As we did for w , we plot J near the PX-point versus time in Figure 5 (see the dotted curve). The curve shows that J starts increasing significantly after $t = 26.8$ when the first O-point commences to form. Therefore, time $t = 26.8$ separates slow and fast evolution stages. By time $t = 29.4$, J at the PX-point increases rapidly to around 265, which is an order of magnitude higher than its initial value. After that, J decreases slowly as a result of the diffusion of the magnetic field through reconnection.

3.2. Formation and Motion of Plasma Blobs

Following the formation of the first X-point (or the PX-point), magnetic reconnection successively creates closed field lines (flare loops) below the PX-point. At $t = 26.8$, the first O-type neutral point (or magnetic island) starts to form above the PX-point at $z = 0.61$, representing the ignition of the tearing

mode instability in the current sheet. Figure 4 shows the distribution of several variables in the x - z plane at time $t = 26.8$ (first row) and $t = 34.0$ (second row), respectively. These variables include the magnetic field together with ρ (left panel), J (left middle panel), v_x (right middle panel), and v_z (right panel). Carefully tracking the evolution of each of these variables, we notice that J continues to increase in the progress of the PX-point formation, and the maximum value of J occurs at the PX-point. This indicates that magnetic reconnection has begun and the fastest reconnection takes place at the PX-point.

However, what happens to the mass is different. The mass density inside the sheet remains almost unchanged in this stage. With the decrease in the sheet thickness, the mass was continuously expelled out of the sheet in two directions (see the contours of v_z in the right panel of Figure 4). The process continues until the first O-point forms above the PX-point at $z = 0.61$ after $t = 26.8$. We identify time $t = 26.8$ with the moment when the tearing mode begins. Following its formation, the first O-point moves upward and leaves the PX-point quickly due to the reconnection outflow. The mass density inside the sheet reaches a dynamical balance with the outside, and the conjugate reconnected magnetic field line at the opposite side of the X-point forms a new flare loop and leaves the X-point quickly as well because of the loop shrinkage that has long been reported in both observations (e.g., Švestka et al. 1987; Forbes & Acton 1996; Vrřnak et al. 2004, and references therein) and theories (Lin et al. 1995, 2004, and references therein).

In the same stage, as shown by velocity contours in the right middle panel of the first row in Figure 4 as well as in the associated movies, plasma inflows outside the sheet are faster near the PX-point than at the other locations, and they are always symmetric with respect to the PX-point. The region where the inflow speed value ($|v_x|$) reaches its maximum rapidly expands in both x - and z -directions as the first O-point forms, and it bifurcates into two as the O-point leaves the PX-point. One of the two regions moves with the O-point, and another one stays on the top of flare loops. In the process, the maximum value of the inflow velocity continues to increase from 0.01 to about 0.1. Simultaneously, the outflow speed v_z increases faster than the inflow speed. Unlike the inflow speed, however, the speed of the outflow along the sheet is not symmetric with respect to the PX-point such that the upward outflow is roughly two times faster than the downward outflow until the first O-point forms. For example, the speeds of both outflows increase from zero as the evolution begins. That of the upward flow reaches 0.24 and that of the downward flow reaches 0.12 as the O-point appears. Then the speed of the downward flow quickly increases, and it eventually catches up with that of the upward flow as the first O-point fully forms.

The second O-point starts to form below the PX-point at around $t = 29.8$, and the third one appears above the PX-point after $t = 30.2$. By the time $t = 34.0$, a series of O-points (plasmoids, plasma blobs, or magnetic islands) has formed in the current sheet. With these new plasmoids forming, multiple X-points are created between every pair of plasmoids. The lower row of Figure 4 shows that some plasma blobs with denser material are located at heights $z = 0.57, 0.70, 1.03, 1.11,$ and 1.53 . Meanwhile, the PX-point is also moving upward at a speed apparently lower than that of the other X- and O-points.

3.3. Kinematics of Plasma Blobs

As we can see from velocity panels in the lower row of Figure 4, motions of plasma blobs and the reconnection outflow

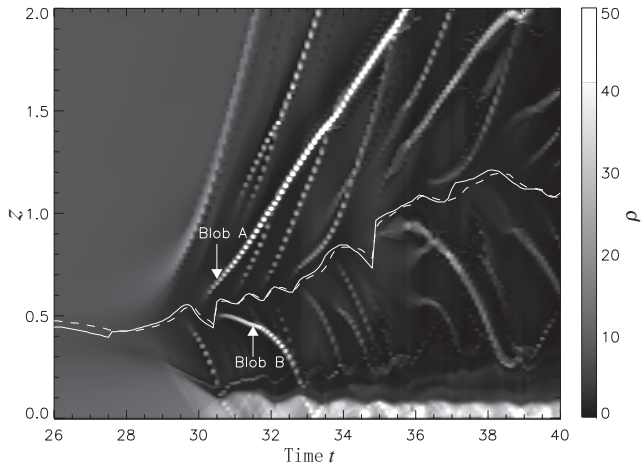


Figure 6. Plasma density (gray scale) and locations of several well-recognized plasma blobs (white solid circles) along the z -axis as functions of time. Two specific blobs, Blob A and Blob B, which are mentioned in the text extensively, are marked. Locations of the S- and PX-points are plotted with dashed and solid curves, respectively.

(An animation of this figure is available in the online journal.)

are completely mixed with one another, and they manifest rich kinematic features. For the convenience of showing their motions, we identify several blobs in the sheet and plot their locations along the sheet (or on the z -axis due to the symmetry) versus time in Figure 6. The background of this plot is black and each bright dot represents a blob. Blobs A and B are two specific examples of these blobs such that Blob A is moving upward and Blob B is moving downward.

In addition, we also plot locations of the PX- and S-points at various times in Figure 6, in which the solid curve is for the PX-point and the dashed one is for the S-point. We noticed that these two special points are not co-located in space although they are very close to one another, as suggested by Seaton (2008), Oka et al. (2008), T. G. Forbes (2009, private communications), and Murphy (2010). Figure 6 shows clearly that motions of blobs bifurcate at the region where these two points are located. Those moving upward eventually leave the domain of the experiment through the open top boundary. For example, Blob A leaves the domain at around $t = 35$. Because the bottom boundary condition is line-tied and the end of each field line there is fixed, reconnected magnetic flux is accumulated above the boundary creating flare loops, and plasma blobs moving downward will thus eventually stop their motions at the top of flare loops. For example, Blob B collides with the closed flare loop beneath and stops its motion at $t = 33$.

Motions of blobs also manifest accelerations, and that of the upward motion is higher than that of the downward motion. For example, Blob B forms near $z = 0.28$, starts moving at a small velocity at around $t = 30.5$, and continues to speed up until it hits the closed field lines at $t = 32.8$ when its velocity reaches $v = 0.4$. At the same time, the height of the loop top is about $z = 0.18$. From its formation at $t = 30.5$ to its collision with the loop top at $t = 32.8$, the lifetime of Blob B is short and is only around $\Delta t = 2.3$.

Blobs moving upward are accelerated more rapidly. More information is revealed by them since they have significantly more room to move. Both Figure 6 and the associated movie clearly indicate that merging occurs frequently among these blobs. For example, in the motion of Blob A, at least three blobs created later successively catch up and merge with it at

Table 2
Speed (km s^{-1}) of Plasma Blobs Observed in Various Situations

Reference	Sunward Blobs	Anti-Sunward Blobs
This work	89–159	147–242
McKenzie & Hudson (1999)	100–200	
Sheeley & Wang (2002)	50–100	
Ko et al. (2003)		140–650
Raymond et al. (2003)		1000
Asai et al. (2004)	100–250	
Sheeley et al. (2004)	100–600	
Lin et al. (2005)		460–1075
Vršnak et al. (2009)		100–1000
Milligan et al. (2010)	12	
Nishizuka et al. (2010)		250–1000
Savage et al. (2010)	21–165	280–460

$t = 31.8$, $t = 33.5$, and $t = 35.4$, respectively. The velocity of the resultant blob following the merging remains almost unchanged although the blobs catching up with the initial Blob A moved significantly faster than Blob A before merging. From the plot in Figure 6, we can deduce the average speed of Blob A before and after merging, which is around 0.41. This time interval in which merging occurs roughly covers the process of formation and disappearance of Blob B as shown by Figure 6.

Besides the motion of blobs in the z -direction, we also notice the motion of the reconnected plasma outside blobs. It is very interesting such that, along the motion direction, the plasma behind a blob may flow faster than this blob, and it quickly slows down when it gets close to the blob. In Figure 7, we plot the plasma velocity distribution along the z -axis at time $t = 26.8$ (solid curve) and $t = 34.0$ (dashed curve), respectively, corresponding to the plots in Figure 4. The two curves in Figure 7 show that the plasma speeds vary smoothly along the z -axis before the formation of blobs. Following the formation of blobs, however, flow patterns fluctuate and change, especially around individual blobs, and plasma outside blobs may flow faster than blobs at some specific locations.

To describe this phenomenon more clearly, we also specify the locations of some blobs at $t = 34.0$ (see the arrows) on the dashed curve and their velocities (see the positive and negative numbers). For the upward flow, for example, we identified three blobs that are located near $z = 1.0$ and $z = 1.5$. The two blobs near $z = 1.0$ have velocities $v = 0.46$ and $v = 0.28$, but the plasma behind (or below) them flows significantly fast. For example, the blob near $z = 1.5$ moves at speed $v = 0.30$, and the reconnected plasma flow behind could move at speeds up to $v = 0.8$. The same situation occurs in the downward flow. Two blobs moving downward have been identified near $z = 0.5$ and $z = 0.7$, which move at speeds of $v = -0.17$ and $v = -0.30$, respectively, and the plasma flow behind (or above) them moves at speeds up to $v = -0.65$ and $v = -0.50$, respectively.

According to the characteristic values given in Equation (11), the above values of the speed of the plasma blobs inside the reconnection outflows range from 147 to 242 km s^{-1} for those in the upward flow, and from 89 to 159 km s^{-1} for those in the downward flow. Obviously, the upward motion is faster than the downward motion, which is consistent with that deduced from observations. Table 2 lists all the results about the speed of the plasma blob observed in various situations that we are able to collect. These results indicate that, in general, the anti-sunward blobs move faster than the sunward ones, and apparently the former is much faster than the latter. This is probably due to the fact that the closed flare loop below the

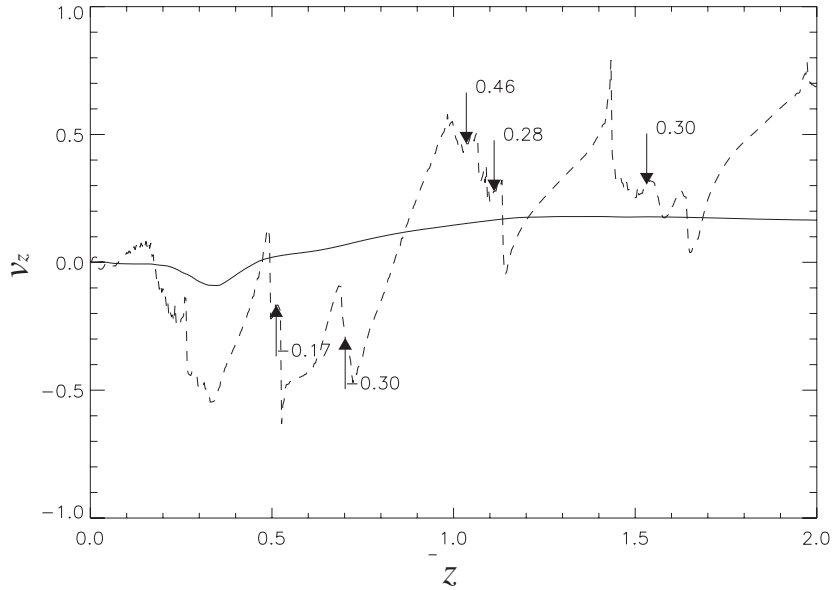


Figure 7. Plasma velocity v_z distribution along the z -axis. The solid curve is for v_z at $t = 26.8$, and the dashed one is for v_z at $t = 34.0$. The arrows indicate positions of some well-recognized plasma blobs along the z -axis, and their instant speeds are specified by those numbers.

current sheet constitutes an obstacle to the motion of the plasma blob. Comparing our results with observational ones indicates that the present experiment displays an intermediate case as a result of a relatively weak background magnetic field (10 G) and high plasma β (~ 0.1).

3.4. Motions of the S-point and the PX-point

As we mentioned earlier, Figure 6 also plots positions of the S- and PX-points on the z -axis as functions of time. The dashed curve is for the S-point, near which the reconnection outflow is roughly static, and the solid curve is for the PX-point, near which the magnetic field almost vanishes and the reconnection rate reaches maximum. These two curves display the overall motion pattern of the S- and PX-points, which are upward, and a couple of smooth fluctuations are also seen. The two points move apparently slower than blobs, but the formation of blobs causes their motions to speed up. This scenario is consistent with the fact that the formation of blobs inside the current sheet accelerates the reconnection process and yields quicker production, accumulation, and growth of flare loops below the two points. It is the growth of the flare loop that pushes the two points upward.

As seen in Figure 6, the S- and PX-points are in general not co-located, and their relative positions switch back and forth as reconnection progresses. The initial motion of the two points is smooth, with the S-point above the PX-point. Following the appearance of blobs at $t = 26.8$, the relative positions of the two points begin to fluctuate. This pattern of motion is seen more clearly in Figure 8, which shows the distance between the PX-point and the S-point versus time. From Figures 6 and 8, it is apparent that the direction in which a plasma blob moves is related to the relative positions of the S- and PX-points. When the S-point is above the PX-point, newly appearing blobs move upward. When the S-point is below the PX-point, newly appearing blobs move downward. Because new blobs are not observed to appear in the short distance between the S-point and PX-point, this implies that plasma blobs never go through the PX-point.

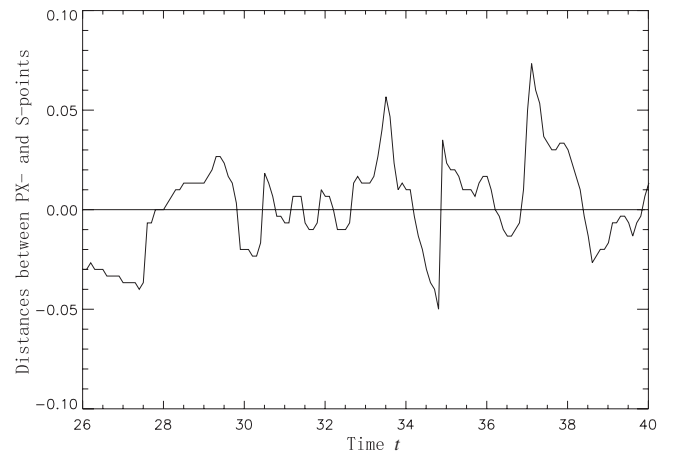


Figure 8. Distances to the S-point as a function of time. The horizontal line is for the S-point itself, and the curve is for the PX-point.

3.5. The Rate of Magnetic Reconnection

Another important parameter for the reconnection process is the rate of magnetic reconnection, M_A , which is the Alfvén Mach number of the reconnection inflow and is defined as the inflow velocity, v_i , near the current sheet compared to the local Alfvén speed, v_A :

$$M_A = \frac{v_i}{v_A}. \quad (23)$$

After multiple X-points appear in the nonlinear phase of the evolution, the magnetic reconnection process displays violent and nonlinear characteristics, and M_A is not necessarily a constant along the current sheet. Figure 4 suggests that M_A reaches its maximum near the PX-point. This is consistent with observations of the reconnection processes taking place in the magnetosphere and other numerical experiments in various environments (e.g., see also discussions of Lin et al. 2008 and references therein for more details). Therefore we focus on the behavior of M_A near the PX-point. To obtain M_A , we locate a small square with a side length of 0.1 right to the PX-point and

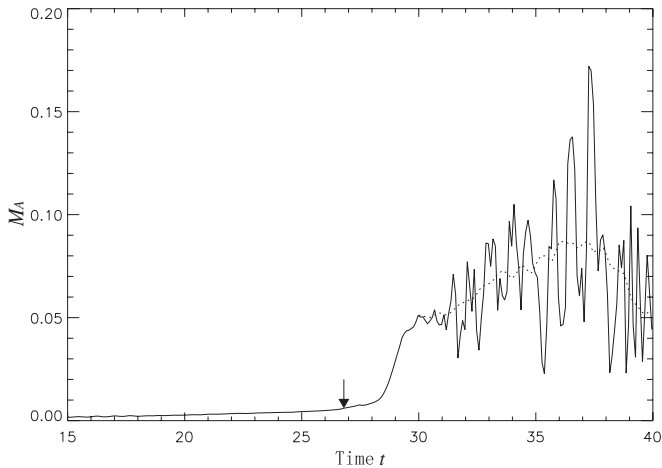


Figure 9. Rate of magnetic reconnection M_A near the PX-point as a function of time. The solid line shows the instant value and the dotted line is for the corresponding average value. The arrow indicates time $t = 26.8$ when the first magnetic island forms.

evaluate v_i and v_A on average over the square. As suggested in Figure 4, v_i is actually identified with v_x near the PX-point.

Figure 9 plots M_A at the PX-point as a function of time. An overall feature of the curve is that M_A increases slowly in the early phases and manifests significant increases after plasma blobs appear in the current sheet. As Figure 9 shows, M_A remains less than 0.01 until $t = 28.0$ when the first blob forms. Then it jumps to 0.05 within a very short period from $t = 28.0$ to $t = 29.6$. Consequently, it evolves in a violent fluctuating fashion such that its maximum value reaches 0.17 and its minimum value drops to 0.023. This is probably due to the impact of the development of the blob. No observation or in situ measurement of the reconnection process in space manifested this behavior of M_A . That may be due to poor spatial resolution in the relevant observations and measurements, but recent numerical experiments display such a feature quite often (e.g., see Skender & Lapenta 2010; Shepherd & Cassak 2010, and references therein). In this period, its average value gradually increases from 0.05 at $t = 29.6$ to 0.085 at $t = 37.0$ (see the dotted curve in the plot). After $t = 37.0$, reconnection becomes slow again because the magnetic fields weaken after most of the magnetic energy has been released.

3.6. Scaling Law for Current Sheet Thickness

To further improve our understanding and knowledge about the impact of the tearing mode and the associated turbulence on various properties of the reconnecting current sheet, we check the scaling law for the current sheet thickness deduced by Lin et al. (2007, 2009) on the basis of the results obtained in the present work. According to the classical theory of the tearing mode instability (Furth et al. 1963), the tearing mode develops within the timescale τ which is shorter than the classical diffusion timescale τ_d and is longer than the Alfvén timescale τ_A (see also Priest & Forbes 2000, pp. 177–189). This directly yields the following constraints on the wave number k and the sheet half-thickness w (see also Lin et al. 2007):

$$S^{-1/4} < \bar{k} < 1, \quad (24)$$

where $\bar{k} = kw$, and $S = \tau_d/\tau_A$ is the Lundquist number (or the magnetic Reynolds number; in fact $R_m = S$) near the current sheet. Lin et al. (2007) further showed that $M_A = S^{-1}$. To

help determine the lower limit to the observed w in order to remove projection effects to the greatest extent from the observational results for w , Lin et al. (2007, 2009) related w_{\min} to M_A and the wavelength of the tearing mode λ , which is identified with the distance between two adjacent plasma blobs flowing along the current sheet in the same direction. The relationship can be summarized in the form below

$$w_{\min} = M_A^\alpha \frac{\lambda}{2\pi} \quad (25)$$

for different types of tearing modes and different boundary conditions. Here α is a dimensionless parameter between 0 and 1.

Loureiro et al. (2007) and Ni et al. (2010) found that a Sweet–Parker current sheet with a large aspect ratio is unstable to the long wave perturbation in a high Lundquist number environment, and the maximum growth rate of the instability in the linear stage is related to the Lundquist number in terms of $S^{1/4}v_A/L_{cs}$, where L_{cs} is the length of the current sheet used in these works. The related numerical simulations suggest that the critical value of the aspect ratio for the tearing mode is about 10^2 in the case of $S = 10^4$ (see Loureiro et al. 2005), and the number of plasmoids appearing inside the current sheet in a given time interval at the linear stage is found to scale as $S^{3/8}$ (Loureiro et al. 2007; Ni et al. 2010). In the nonlinear regime, the reconnection rate is nearly independent of S , and the number of plasmoids is roughly proportional to S (Bhattacharjee et al. 2009; Huang & Bhattacharjee 2010).

Huang & Bhattacharjee (2010) also found that the thickness of the sheet is related to the scale of the system, L , as $LR_{mc}^{1/2}/R_m$, where R_{mc} is the critical value of the magnetic Reynolds number at which the plasmoids start to appear in the reconnecting current sheet. In their experiments, R_m is between 5×10^5 and 2×10^6 , and $R_{mc} = 4 \times 10^4$. This brings the scale of the sheet thickness into the range $10^{-4}L$ to $4 \times 10^{-4}L$. Comparing our results shown in Figure 5 and those deduced from Equation (25) indicates that the sheet thickness of Huang & Bhattacharjee (2010) is at least an order of magnitude smaller than what we have obtained in the present work. Therefore, the difference between the results of the two works is apparent.

However, we need to note that the analyses and results of other works mentioned above were conducted and obtained in symmetric configurations. Obviously, the reconnection occurring in either the solar eruption or in the geomagnetic tail is not in a symmetric configuration. Instead the evolution in the magnetic field is subject to the condition of line-tying to the bottom surface and no restriction is imposed on the field in other directions. Therefore, both the tearing mode and the plasmoid instabilities studied here should behave differently from those taking place in the cases investigated by Loureiro et al. (2007), Bhattacharjee et al. (2009), Huang & Bhattacharjee (2010), and Ni et al. (2010), and we do not expect the same scaling law found in this work as those for the cases of the symmetric configuration to exist.

Following the practice of Lin et al. (2007, 2009), in this work we take λ as the distance between two adjacent plasma blobs after they are fully formed and recognizable, M_A is measured near the PX-point so that it can be estimated from Figure 9, and w_{\min} is measured at the middle point between the two corresponding blobs. From Figures 4 and 6, we track the blobs moving upward because Lin et al. (2007, 2009) tracked those leaving the Sun. We identified three pairs of such blobs, and plot

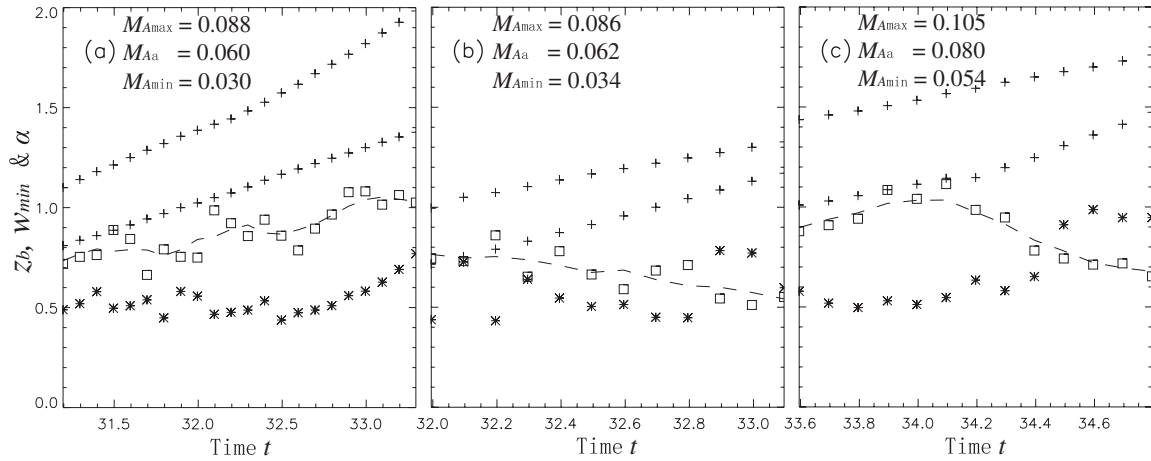


Figure 10. Locations of the selected pairs of upward moving blobs along the z -axis, z_b (symbol “+”), values of w_{\min} of a piece of the current sheet between the corresponding selected two blobs (symbol asterisk), and values of α (symbol square) as functions of time for three cases: (a) in the time interval between $t = 31.2$ and $t = 33.3$, the two blobs are separating; (b) in the period from $t = 32.0$ to 33.1 , the two blobs are approaching one another; and (c) in the period from $t = 33.6$ to 34.8 , the two blobs are approaching one another. In each panel, the dashed curve is the fit to the values of α , and the maximum, minimum, and average of M_A are displayed in the upper left corner.

their locations, z_b , on the z -axis versus time in Figure 10 (see symbol “+” in the figure).

Figure 10(a) displays the locations of a pair of blobs in the time interval between $t = 31.2$ and $t = 33.3$. In this period, their distance λ gradually increases from 0.29 to 0.61, the corresponding values of M_A vary from 0.03 to 0.088, and w_{\min} varies from 0.0048 to 0.007. Substituting these values into Equation (25) brings α into the range 0.70–1.08 (see the squares in Figure 10(a); the dashed line is the fit to the results). Figures 10(b) and (c) are for the cases of two blobs approaching one another as they move in the sheet. Figure 10(b) covers the period from $t = 31.8$ to $t = 33.2$, M_A ranges from 0.034 to 0.086, λ is from 0.16 to 0.3, and w_{\min} ranges from 0.004 to 0.007. We find that α is between 0.50 and 0.86, and it tends to decrease as two blobs merge with one another. Figure 10(c) shows a situation similar to that in Figure 10(b) and covers the period from $t = 33.6$ to $t = 35.0$. In this period, λ is between 0.29 and 0.45, M_A changes in the range from 0.054 to 0.105, and w_{\min} varies from 0.005 to 0.01. Therefore, we deduce α according to Equation (25) such that $0.65 < \alpha < 1.12$.

In the above three cases, Figure 10(a) is for the case in which two blobs are moving apart, and the largest distance between them is $\lambda = 0.61$, which is the largest one of two adjacent blobs that we can track within the calculation domain. Figures 10(b) and (c) are the example of two blobs merging with one another. In these two cases, we note that we chose smaller values of λ , 0.29 and 0.16, respectively, in an arbitrary fashion, instead of $\lambda = 0$ when two of them completely merge together. This is because the turbulence developed by the tearing mode is still in the linear stage prior to the merging of the two blobs and Equation (25) holds. Whether Equation (25) still remains valid as two blobs totally merge or even as they become very close to one another is an open question, and will be investigated in future work.

What we have found so far from three examples indicates that $0.50 < \alpha < 1.12$. Our results also show that α tends to decrease with λ . This probably has something to do with the fact that the value of w between two adjacent blobs in the present experiment remains almost unchanged. Consulting the work by Lin et al. (2009) which gave a value of α between $1/7$ and 1, we conclude that the range of α values deduced in this work is consistent

with theirs, which can be considered a confirmation of their theoretical results by the numerical experiment performed here.

4. DISCUSSION AND CONCLUSIONS

This work is a follow-up to those of Forbes & Priest (1983) and Forbes & Malherbe (1991). We performed a set of numerical experiments for magnetic reconnection taking place in the two-ribbon flare processes. The resistive MHD equations were solved using the modified SHASTA code (see also Shen & Lin 2009, 2010). In this work, the code was modified in two ways. First of all, it was improved by simply increasing the number of grid points in the experiment domain. This is the simplest and most straightforward approach to enhancing the resolution of experiments. It is usually used in cases where the computational resource is rich, and the CPU time and computation speed are guaranteed. The other advantage of this approach is that it does not introduce additional errors into the calculation.

The second approach we tested here is of the so-called AMR technique, which allows the code to adjust the size of the grid automatically in the region where the gradients of variables exceed a threshold. This technique requires extra effort in modifying the structure of the code, and is usually used when the computational resources are limited and the efficiency of using facilities is an important issue. When other conditions are unchanged, we ran the modified SHASTA code improved in two ways for the same problem and found that the code modified by AMR is indeed more efficient than that modified by simply increasing the grid number. However, applying the AMR technique might introduce additional errors into calculations. Therefore, we need to be very careful when applying the AMR technique to the code.

Using the modified code, we studied the evolutionary features of the reconnecting current sheet that is supposed to occur in two-ribbon flares. Generally, our experiments duplicate the main features of the current sheet shown in previous experiments by Forbes & Priest (1983) and Forbes & Malherbe (1991), for example, thinning of the sheet, formation of multiple X- and O-points, and growth of the post-flare loops. Because of the much higher R_m and much larger N_g used than before, however, more details of the reconnection process were displayed, and thus many new features were shown by the experiment.

The main results of this work are summarized as follows.

1. Whether or not the tearing mode takes place in a long current sheet depends in an important way on the value of R_m (see also the result of Samtaney et al. 2009). In cases of small R_m , the dissipation of the magnetic field through the current sheet occurs fast enough that no features of the tearing mode appear. In cases of large R_m , however, as expected, magnetic islands or plasma blobs form in the current sheet as the sheet gets thinner, but the situation is not completely the same as predicted by the standard theory of the tearing mode (Furth et al. 1963) such that the mode develops when the length-to-thickness ratio of the sheet exceeds 2π . Instead the sheet studied in the present work extends upward from $y = 0$ to infinity; it evolved gradually until the electric current exceeded a threshold value, then magnetic islands or plasma blobs began to appear, representing the initiation of the tearing mode instability. This is consistent with what other numerical experiments have found (e.g., see Ni et al. 2010 and references therein).
2. The plasma density inside the current sheet is initially high compared to that outside. As the sheet becomes thinner, the density decreases. The density inside the sheet becomes comparable to that of the surroundings when the magnetic island appears and the tearing mode occurs. This seems to suggest that high density inside the sheet is a factor that prevents tearing from occurring, but this needs to be checked in the future.
3. Contrary to expectations, thinning of the sheet does not take place uniformly along the whole sheet. Instead it mainly happens at a specific location which eventually develops into the PX-point when multiple X- and O-points (or islands) appear. This evolutionary behavior of the sheet has something to do with the fact that the magnetic field in the configuration is line-tied, with one end fixed to the boundary surface, so different parts of individual field lines are not allowed to move with equal freedom. Such a scenario has already been shown by many observations of eruptions in the solar atmosphere and in situ measurements of substorms in the geomagnetic environment (e.g., see Savage et al. 2010 and discussions of Lin et al. 2008).
4. Formation of the PX-point is followed by the appearance of multiple X- and O-points in the sheet. These secondary X- and O-points do not stay where they form. Instead they move along the sheet either upward or downward (refer to Riley et al. 2007 for similar results). Simultaneously, closed field lines where flare loops are supposed to lie are created below the PX-point as a result of magnetic reconnection and line-tying of field lines at the boundary. The blobs moving downward eventually collide with the closed loops, change their kinematic behavior, and produce a termination shock on the top of flare loops (e.g., see also Forbes & Acton 1996 for more discussion). They are observed at low altitudes by *Yohkoh*, the Solar Ultraviolet Measurement of Emitted Radiation, *TRACE*, *RHESSI*, and *Hinode* (e.g., see McKenzie & Hudson 1999; McKenzie 2000; Yokoyama et al. 2001; Innes et al. 2003; Asai et al. 2004; Sheeley & Wang 2002; Reeves et al. 2008; Milligan et al. 2010; Savage et al. 2010). The blobs moving upward eventually leave the calculation domain due to the open boundary condition. They are apparently observed at high altitudes by LASCO and the Ultraviolet Coronagraph Spectrometer (e.g., see Ko et al. 2003; Lin et al. 2005, 2009; Savage et al. 2010).
5. An interesting phenomenon revealed by our experiment, but not yet confirmed by observations, is that in the same direction, the plasma behind a blob may flow faster than the blob and quickly slows down when it gets close to the blob. Plasma blobs flowing anti-sunward are apparently faster than those flowing sunward, which is generally consistent with observations. This is because the closed flare loops prevent blobs from moving fast in the sunward direction. For the characteristic values of important parameters used in this work, the plasma blob moves anti-sunward at speeds ranging from 147 to 242 km s⁻¹, and moves sunward at speeds from 89 to 159 km s⁻¹.
6. In the early stages of evolution in the system, neither reconnecting electric current density J nor the rate of magnetic reconnection M_A has a large value. Instead they increase slowly until they form magnetic islands in the sheet. The appearance of the chain of magnetic islands is followed by a quick enhancement in both M_A and J , implying a significant role of the formation of magnetic islands or the initiation of the tearing mode in promoting fast magnetic reconnection.
7. Blobs moving in different directions bifurcate at the so-called S-point, which is very close to the PX-point, but is not co-located with the PX-point in space. This result has been shown previously by other experiments (T. G. Forbes 2010, private communications; and see also Seaton 2008; Oka et al. 2008; Murphy 2010). Both S- and PX-points move upward gradually with the growth of the loop system beneath. However, the relative locations of these two points change with time and alternate back and forth. The direction of motion of blobs is related to the relative position of these two points. Newly formed blobs move upward if the S-point is above the PX-point and downward if the S-point is below the PX-point. This implies that the paths of individual blobs do not cross the PX-point. Occasionally, blobs moving in the same direction merge with each other.
8. Tracking three pairs of blobs that all move upward, we noticed that the length of a piece of the current sheet between each pair λ , the half thickness w of the same piece of the sheet, and the rate of magnetic reconnection M_A satisfy the scaling law deduced by Lin et al. (2009) for a current sheet in which the tearing mode is developing. This indicates that many features of the CME/flare current sheet observed so far could be well related to the development of the tearing mode.

The authors acknowledge useful discussions with J. C. Raymond and T. G. Forbes. This work was supported by Program 973 grant 2011CB811403, NSFC grant 10873030, and CAS grant 2009J2-34. J.L. and N.M. acknowledge support from NASA grant NNX11AB61G to SAO, and from a grant from the Smithsonian Institution Sprague Endowment Fund during FY10. Some important calculations in this work were completed with the help of the HPC Center, Kunming Institute of Botany, CAS.

REFERENCES

- Asai, A., Yokoyama, T., Shimojo, M., & Shibata, K. 2004, *ApJ*, 605, L77
 Bárta, M., Vršnak, B., & Karlický, M. 2008, *A&A*, 477, 649
 Bemporad, A., Poletto, G., Suess, S. T., Ko, Y.-K., Schwadron, N. A., Elliott, H. A., & Raymond, J. C. 2006, *ApJ*, 638, 1110
 Bettarini, L., & Lapenta, G. 2010, *A&A*, 518, 57
 Bhattacharjee, A., Huang, Y.-M., Yang, H., & Rogers, B. 2009, *Phys. Plasmas*, 16, 112102

- Boris, J. P., & Book, D. L. 1973, *J. Comput. Phys.*, **11**, 38
- Boris, J. P., & Book, D. L. 1976, *J. Comput. Phys.*, **20**, 397
- Cargill, P. J., & Priest, E. R. 1982, *Sol. Phys.*, **76**, 357
- Carmichael, H. 1964, in *The Physics of Solar Flares*, ed. W. N. Hess (NASA Special Publication, Vol. 50; Washington, DC: NASA), 451
- Ciaravella, A., & Raymond, J. C. 2008, *ApJ*, **686**, 1372
- Ciaravella, A., Raymond, J. C., Li, J., Reiser, P., Gardner, L. D., Ko, Y.-K., & Fineschi, S. 2002, *ApJ*, **575**, 1116
- Daughton, W., Scudder, J., & Karimabadi, H. 2006, *Phys. Plasmas*, **13**, 072101
- Forbes, T. G. 2000, *J. Geophys. Res.*, **105**, 23153
- Forbes, T. G., & Acton, L. W. 1996, *ApJ*, **459**, 330
- Forbes, T. G., & Lin, J. 2000, *J. Atmos. Sol.-Terr. Phys.*, **62**, 1499
- Forbes, T. G., & Malherbe, J. M. 1991, *Sol. Phys.*, **135**, 361
- Forbes, T. G., & Priest, E. R. 1983, *Sol. Phys.*, **84**, 169
- Furth, H. P., Killeen, J., & Rosenbluth, M. N. 1963, *Phys. Fluids*, **6**, 459
- Hirayama, T. 1974, *Sol. Phys.*, **34**, 323
- Huang, Y.-M., & Bhattacharjee, A. 2010, *Phys. Plasmas*, **17**, 062104
- Innes, D. E., McKenzie, D. E., & Wang, T. 2003, *Sol. Phys.*, **217**, 247
- Ko, Y.-K., Raymond, J. C., Lin, J., Lawrence, G., Li, J., & Fludra, A. 2003, *ApJ*, **594**, 1068
- Kopp, R. A., & Pneuman, G. W. 1976, *Sol. Phys.*, **50**, 85
- Lin, J. 2002, *Chin. J. Astron. Astrophys.*, **2**, 539
- Lin, J., Cranmer, S. R., & Farrugia, C. J. 2008, *J. Geophys. Res.*, **113**, 11107
- Lin, J., & Forbes, T. G. 2000, *J. Geophys. Res.*, **105**, 2375
- Lin, J., Forbes, T. G., Priest, E. R., & Bungey, T. N. 1995, *Sol. Phys.*, **159**, 275
- Lin, J., Ko, Y.-K., Sui, L., Raymond, J. C., Stenborg, G. A., Jiang, Y., Zhao, S., & Mancuso, S. 2005, *ApJ*, **622**, 1251
- Lin, J., Li, J., Forbes, T. G., Ko, Y.-K., Raymond, J. C., & Vourlidas, A. 2007, *ApJ*, **658**, L123
- Lin, J., Li, J., Ko, Y.-K., & Raymond, J. C. 2009, *ApJ*, **693**, 1666
- Lin, J., Raymond, J. C., & van Ballegooyen, A. A. 2004, *ApJ*, **602**, 422
- Lin, J., Soon, W., & Baliunas, S. L. 2003, *New Astron. Rev.*, **47**, 53
- Loureiro, N. F., Cowley, S. C., Dorland, W. D., Haines, M. G., & Schekochihin, A. A. 2005, *Phys. Rev. Lett.*, **95**, 235003
- Loureiro, N. F., Schekochihin, A. A., & Cowley, S. C. 2007, *Phys. Plasmas*, **14**, 100703
- Martens, P. C. H., & Kuin, N. P. M. 1989, *Sol. Phys.*, **122**, 263
- McKenzie, D. E. 2000, *Sol. Phys.*, **195**, 381
- McKenzie, D. E., & Hudson, H. S. 1999, *ApJ*, **519**, L93
- Milligan, R. O., McAteer, R. T. J., Dennis, B. R., & Young, C. A. 2010, *ApJ*, **713**, 1292
- Murphy, N. A. E. 2010, *Phys. Plasmas*, **17**, 112310
- Ni, L., Germaschewski, K., Huang, Y.-M., Sullivan, B. P., Yang, H., & Bhattacharjee, A. 2010, *Phys. Plasmas*, **17**, 052109
- Nishizuka, N., Takasaki, H., Asai, A., & Shibata, K. 2010, *ApJ*, **711**, 1062
- Oka, M., Fujimoto, M., Nakamura, T. K. M., Shinohara, I., & Nishikawa, K.-I. 2008, *Phys. Rev. Lett.*, **101**, 205004
- Priest, E., & Forbes, T. (ed.) 2000, in *Magnetic Reconnection: MHD Theory and Applications* (Cambridge: Cambridge Univ. Press)
- Raymond, J. C., Ciaravella, A., Dobrzycka, D., Strachan, L., Ko, Y.-K., Uzzo, M., & Raouafi, N.-E. 2003, *ApJ*, **597**, 1106
- Reeves, K. K., et al. 2008, *J. Geophys. Res.*, **113**, A00B02
- Riley, P., Lionello, R., Mikić, Z., Linker, J., Clark, E., Lin, J., & Ko, Y.-K. 2007, *ApJ*, **655**, 591
- Samtaney, R., Loureiro, N. F., Uzdensky, D. A., Schekochihin, A. A., & Cowley, S. C. 2009, *Phys. Rev. Lett.*, **103**, 105004
- Savage, S. L., McKenzie, D. E., Reeves, K. K., Forbes, T. G., & Longcope, D. W. 2010, *ApJ*, **722**, 329
- Seaton, D. B. 2008, PhD thesis, Univ. New Hampshire, Durham
- Sheeley, N. R., Jr., & Wang, Y.-M. 2002, *ApJ*, **579**, 874
- Sheeley, N. R., Jr., Warren, H. P., & Wang, Y.-M. 2004, *ApJ*, **616**, 1224
- Shen, C., & Lin, J. 2009, *Acta Astron. Sin.*, **50**, 391
- Shen, C., & Lin, J. 2010, *Chin. Astron. Astrophys.*, **34**, 288
- Shepherd, L. S., & Cassak, P. A. 2010, *Phys. Rev. Lett.*, **105**, 15004
- Skender, M., & Lapenta, G. 2010, *Phys. Plasmas*, **17**, 2905
- Sturrock, P. A. 1968, in *IAU Symp. 35, Structure and Development of Solar Active Regions*, ed. K. O. Kiepenheuer (Dordrecht: Reidel), 471
- Švestka, Z., Cliver, E. W., Jackson, B. V., & Machado, M. E. 1992, in *IAU Colloq. 133, Eruptive Solar Flares*, ed. Z. Švestka, B. V. Jackson, & M. E. Machado (New York: Springer), 1
- Švestka, Z. F., Fontenla, J. M., Machado, M. E., Martin, S. F., & Neidig, D. F. 1987, *Sol. Phys.*, **108**, 237
- Uzdensky, D. A., Loureiro, N. F., & Schekochihin, A. A. 2010, *Phys. Rev. Lett.*, **105**, 235002
- Vršnak, B., Maričić, D., Stanger, A. L., & Veronig, A. 2004, *Sol. Phys.*, **225**, 355
- Vršnak, B., et al. 2009, *A&A*, **499**, 905
- Weber, W. J., Boris, J. P., & Gardner, J. H. 1979, *Comput. Phys. Commun.*, **16**, 243
- Yokoyama, T., Akita, K., Morimoto, T., Inoue, K., & Newmark, J. 2001, *ApJ*, **546**, L69